Cellular and Molecular Life Sciences (2022) 79:352
https://doi.org/10.1007/s00018-022-04365-4

ORIGINAL ARTICLE

Inhibition of ALG3 stimulates cancer cell immunogenic ferroptosis to potentiate immunotherapy

Pei Liu[1] · Cha Lin[1] · Zheyu Liu[1] · Chenchen Zhu[1] · Zhongda Lin[1] · Dan Xu[1] · Jian Chen[1] · Qian Huang[2] · Chuan-Yuan Li[3] · Linlin Hou[1] · Ji-An Pan[1] · Xinjian Liu[1]

Received: 21 January 2022 / Revised: 27 April 2022 / Accepted: 10 May 2022 / Published online: 8 June 2022

Abstract

Immune checkpoint blockade therapy has drastically improved the prognosis of certain advanced-stage cancers. However, low response rates and immune-related adverse events remain important limitations. Here, we report that inhibiting ALG3, an a-1,3-mannosyltransferase involved in protein glycosylation in the endoplasmic reticulum (ER), can boost the response of tumors to immune checkpoint blockade therapy. Deleting N-linked glycosylation gene *ALG3* in mouse cancer cells substantially attenuates their growth in mice in a manner depending on cytotoxic T cells. Furthermore, ALG3 inhibition or N-linked glycosylation inhibitor tunicamycin treatment synergizes with anti-PD1 therapy in suppressing tumor growth in mouse models of cancer. Mechanistically, we found that inhibiting ALG3 induced deficiencies of post-translational N-linked glycosylation modification and led to excessive lipid accumulation through sterol-regulated element-binding protein (SREBP1)-dependent lipogenesis in cancer cells. N-linked glycosylation deficiency-mediated lipid hyperperoxidation induced immunogenic ferroptosis of cancer cells and promoted a pro-inflammatory microenvironment, which boosted anti-tumor immune responses. In human subjects with cancer, elevated levels of ALG3 expression in tumor tissues are associated with poor patient survival. Taken together, we reveal an unappreciated role of ALG3 in regulating tumor immunogenicity and propose a potential therapeutic strategy for enhancing cancer immunotherapy.

Keywords ALG3 · Immunogenic ferroptosis · Lipid metabolism · Immune checkpoint therapy

Introduction

Glycosylation is a ubiquitous post-translational modification in eukaryotes [1, 2], which starts in the endoplasmic reticulum (ER) and requires activated dolichol precursors for the initial steps. Alpha 1,3-mannosyltransferase (ALG3) catalyzes the first Dol-P-Man-dependent mannosylation step, which is critical for lipid-linked oligosaccharides and protein N-linked glycosylation, at the luminal side of the ER [3, 4]. Previous studies indicated that glycosylation alteration of individual protein might affect cancer progression and metastasis [5, 6]. However, the mechanism of cellular level alternations of N-linked glycosylation, typically ALG3 defects in cancer immunity, remains elusive.

Glycosylation alterations lead to the accumulation of unfolded or misfolded protein in ER, and subsequently triggering an adaptive stress response known as unfolded protein response (UPR-ER) to preserve ER homeostasis [7–9]. Tunicamycin (TM), an inhibitor of N-linked glycosylation, disrupts protein maturation by blocking the transmission of UDP-N-acetylglucosamine to dolichol phosphate in the ER of eukaryotic cells [10].

ER stress increases lipogenesis by the upregulation of genes involved in lipid metabolism [9, 11]. N-linked glycosylation is required for lipid homeostasis, peroxisome biogenesis. For example, N-linked glycosylation of sterol-regulated element-binding protein (SREBP1) cleavage-activating protein (SCAP) is essential for SREBP1 activation,

✉ Xinjian Liu
jnulxj@163.com

1 The Department of Biochemistry and Molecular Cell Biology, Molecular Cancer Research Center, School of Medicine, Sun Yat-Sen University, No. 66, Gongchang Rd, Shenzhen 518107, Guangdong, China

2 Molecular Diagnostic Laboratory of Cancer Center, Shanghai General Hospital, Shanghai Jiaotong University School of Medicine, Shanghai, China

3 Department of Dermatology, Duke University Medical Center, Durham, NC, USA

which is a transcription factor that regulates de novo fatty acid synthesis and polyunsaturated fatty acids (PUFAs) production in mammals [12]. Excessive accumulation of lipid and their intermediate products cause lipotoxicity, leading to cell death [13].

Ferroptosis is an iron-dependent programmed cell death characterized by the accumulation of iron-dependent lethal lipid peroxides [14]. System cystine/glutamate antiporter (system xCT) imports cystine and provides cysteine for the biosynthesis of glutathione (GSH) [15], which is essential for glutathione peroxidase 4 (GPX4) [16, 17]. By interacting with lipids, reactive oxygen species (ROS) also accumulated through a feedback loop initiated by the peroxidation of fatty acids. Once the system xCT/GSH/GPX4 axis is inhibited, a lethal amount of lipid peroxide is accumulated and activated the process of ferroptosis. The interaction of lipid metabolism and ferroptosis modulates cancer initiation [18], development, metastasis, therapy resistance, as well as cancer immunity [19–21]. IFNγ secreted by activated $CD8^+$ T cells promotes ferroptosis of cancer cells, and the ferroptotic cancer cells release lipid metabolites and the high mobility group box 1 (HMGB1) to mediate antitumor immunity [22].

Here, we show that genetic depletion of ALG3 and pharmaceutical inhibition of N-linked glycosylation in murine cancer cells substantially attenuate their growth in mice in a cytotoxic T cell-dependent manner and promote the efficiency of immune checkpoint blockade therapy. Furthermore, we implicate a previously unappreciated mechanism that ALG3-defect induces ER stress and lipogenesis through SREBP1 activation in cancer cells, which induces immunogenic ferroptosis of cancer cells and promotes a pro-inflammatory microenvironment to boost anti-tumor immune response.

Results

ALG3 is identified to play critical roles in human and mouse tumor growth

To identify critical N-linked glycosylation genes in cancers, we first obtained the intersection of glycosylation genes (163 genes) between two published glycosylation-related gene lists (Table S1). One was defined by GeneCards (https://www.genecards.org) according to relevance score (relevance score > 1), and the other was screened out from N-linked glycosylation inhibitor tunicamycin-treated cells [23]. After querying the expression of these intersected genes in multiple tumor samples including skin cutaneous melanoma (SKCM), kidney renal clear cell carcinoma (KIRC), liver hepatocellular carcinoma (LIHC) and low-grade glioma (LGG) from the Cancer Genome Atlas (TCGA), a 137-gene panel was coherently established to represent well-defined N-linked glycosylation processes (Fig. 1a, Table S1). The expression of these 137 genes in SKCM, KIRC, LIHC and LGG were shown in Supplementary Fig. 1a. We then performed univariate Cox regression analysis [24] to confirm the association of the 137-gene panel with patient prognostic value. As shown in Fig. 1b, the survival contribution of individual genes in different cancer types was variable. Some genes in the 137-gene panel, which significantly contributed to the prognosis of the patients in each cancer cohort, were defined as core genes (Table S2) for calculating N-linked glycosylation risk score (G-score). Although there was large difference of glycosylation-related core genes from one cancer type to another (Table S2), it might reflect the critical function of post-translational glycosylation modification to tumor heterogeneity.

Patients from different cancer types were arrayed respectively based on risk scores and categorized into high- and low-risk groups (Supplementary Fig. 1b). Those patients with a higher N-linked glycosylation risk score (G-score) showed a significantly worse overall survival (Supplementary Fig. 1c–f). Interestingly, the N-linked glycosylation core gene list in different cancer types was variable (Table S2), and two genes (*ALG3* and *TMEM147*) were intersected and highlighted in the tested four cancer types (Fig. 1c). Of note, ALG3, a lumenal mannosyltransferases for N-linked glycosylation was expressed in a higher level in tumor tissues than in normal tissues (Supplementary Fig. 1g; Table S3), suggesting that ALG3 may be a critical regulator for tumor growth in multiple cancer types.

To investigate the potential role of ALG3 in tumor growth, we first generated ALG3 knockout human and mouse malignancy cell lines (Supplementary Fig. 1h, i). ALG3 depletion significantly suppresses N-linked glycosylation in these cell lines as expected (Supplementary Fig. 1j, k), with no significantly effect on cell proliferation in vitro (Supplementary Fig. 1l). We then carried out tumor-growth-delay experiments in syngeneic mice inoculated with ALG3-deficient Renca, MC38, B16 and 4T1 tumor cells (Supplementary Fig. 1h, i, m, n). ALG3-deficiency significantly attenuated their abilities to form tumors and prolonged the survival of syngeneic hosts in comparison with those of vector controls. When compared with vector control, knocking out ALG3 significantly attenuated tumor growth and prolonged the survival of host mice in four mouse models (Fig. 1d–k). The results of ALG3 depletion mediated suppression of tumor growth in mice models were consistent with those of N-linked glycosylation score (G score) predicting overall survival of tumor patients. Our data demonstrated that the level of cellular N-linked glycosylation could be a prognosis marker for cancers, and ALG3 might be a novel therapeutic target.

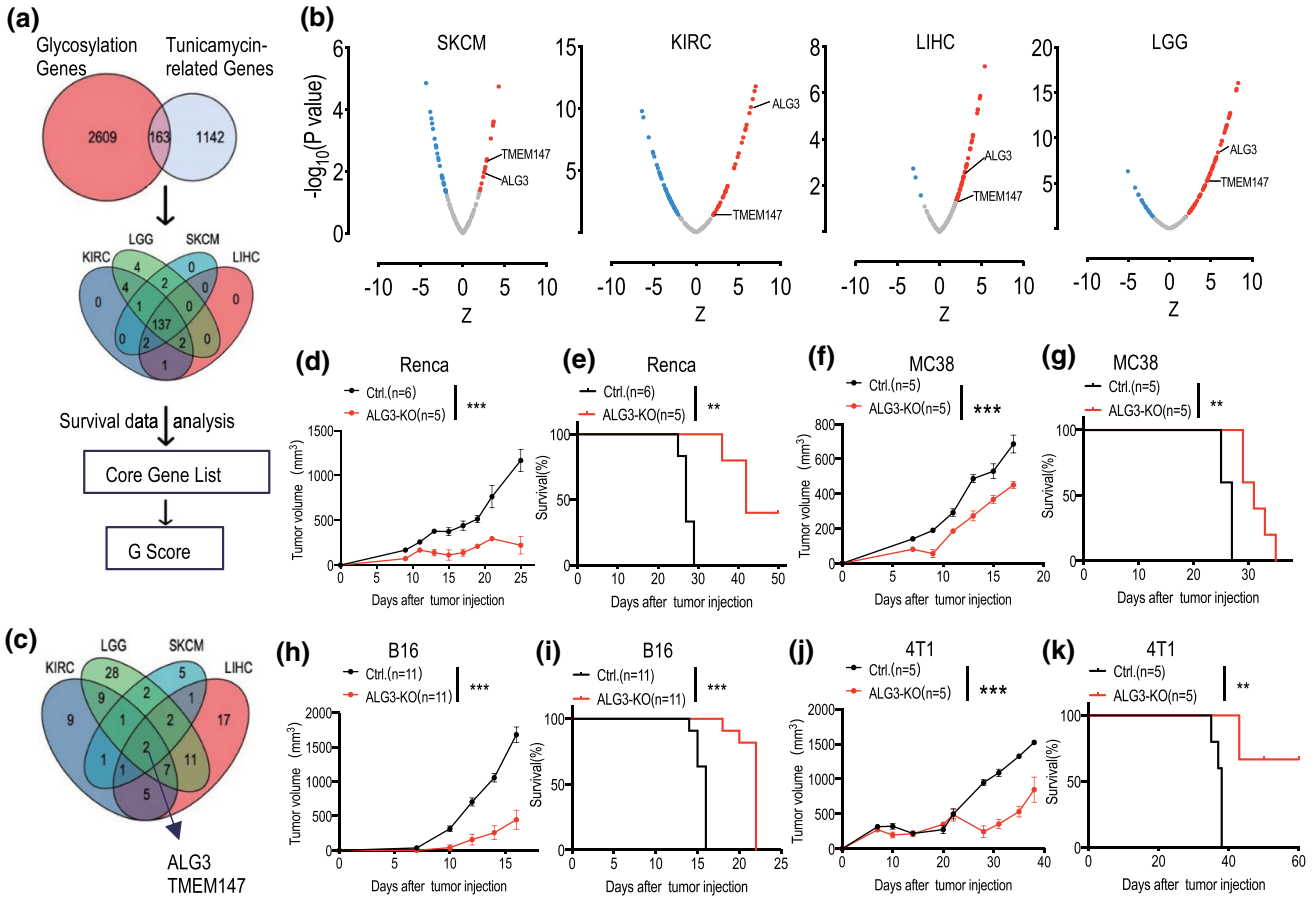

Fig. 1 ALG3 plays critical roles in human and mouse cancer growth. **a** Flowchart of identification N-linked glycosylation core gene-related risk score (G score) by use of public TCGA cohorts. Genes were listed in Table S1. **b** Volcano plots showing the calculated Cox regression models between each of 137 N-linked glycosylation gene expression and overall survival (OS) in TCGA SKCM, KIRC, LIHC, and LGG data set. $Z = \text{coeff}/(\text{se}(\text{coeff}))$, The red dots mean genes expression related to decreased survival and blue ones mean genes related to increased survival, while gray ones mean genes have no significant relationship with survival. **c** Venn diagram plotter showing the increased survival factors in tested four types of cancer. ALG3 and TMEM147 were intersected in tested four types of cancer. Tumor growth curve (**d**) and host mice survival (**e**) of ALG3-KO or Ctrl. Renca kidney adenocarcinoma cell line in Balb/c mice. Tumor growth curve (**f**) and host mice survival (**g**) of ALG3-KO or Ctrl. MC38 colon adenocarcinoma cell line in C57BL/6 mice. Tumor growth curve (**h**) and host mice survival (**i**) of ALG3-KO or Ctrl. B16F10 melanoma cell line in C57BL/6 mice. Tumor growth curve (**j**) and host mice survival (**k**) of ALG3-KO or Ctrl. 4T1 breast cancer cell line in Balb/c mice. Error bars represent mean ± SEM. $^{**}p < 0.01$, $^{***}p < 0.001$. p values by two-way analysis of variance (ANOVA) in **d, f, h, j** and log-rank test in **e, g, i, k**

ALG3 depletion causes excessive lipids accumulation through ER stress-mediated SREBP1 activation

We performed Kyoto Encyclopedia of Genes and Genomes (KEGG) pathway analysis of the intersection genes (163 genes) between two glycosylation-related gene lists. We found the enrichment of signaling pathways including metabolism of protein, asparagine N-linked glycosylation and immune system (Supplementary Fig. 2a). Then we tried to investigate the role of ALG3 on cell metabolism by use of LC–MS/MS-based untargeted metabolomic method (BGI-Shenzhen). As shown in Fig. 2a, the overall metabolic profile of ALG3-deficient cells was significantly different from that of vector control cells. Of the 1376 tested metabolites, there were 153 upregulated and 71 downregulated in ALG3-deficient cells by comparison with those of vector control cells (Fig. 2b). The untargeted metabolomics analysis demonstrated that knocking out ALG3 significantly influenced the metabolism of cancer cells (Supplementary Fig. 2b).

KEGG pathway analysis further indicated that the upregulated metabolites of ALG3 knockout cells were largely involved in the pathways, such as unsaturated fatty acid biosynthesis, glycolysis or gluconeogenesis (Fig. 2c). We then individually examined the expression of SREBP1, a transcription factor that regulates cellular fatty acid metabolism and glycolysis in mammals [25]. Furthermore, we generated ALG3 knockout MDA-MB-231 cell lines

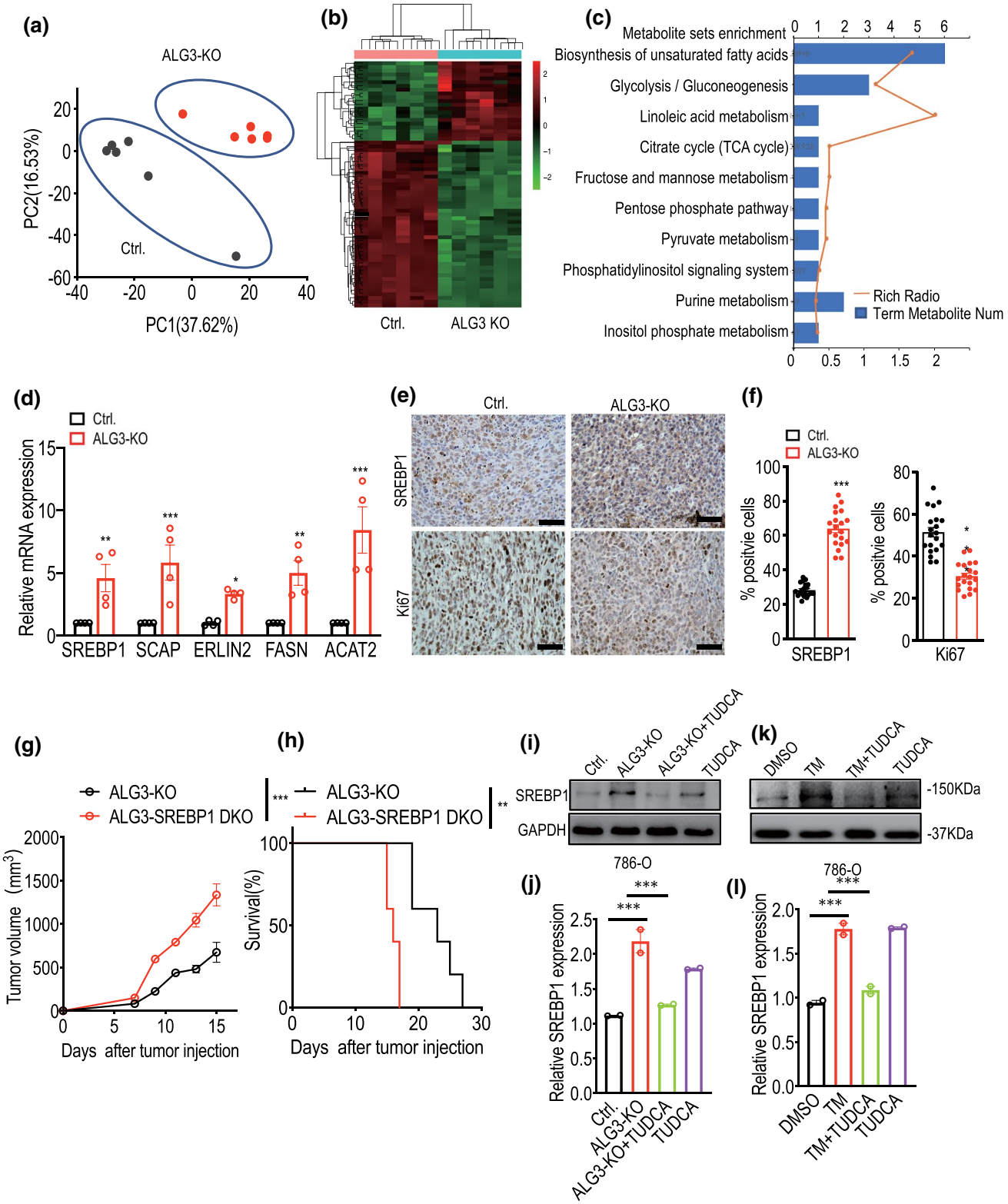

(Supplementary Fig. 2c, d). The expression of other fatty acid synthase genes in ALG3-deficient MDA-MB-231 tumor cells was measured by quantitative real-time PCR (qRT-PCR). Our data showed that the expression levels of fatty acid synthase related genes (*SREBP1, SCAP, ERLIN2, FASN* and *ACAT2*) were significantly evaluated in both mouse and human ALG3-deficient tumor cells compared with those of vector control (Fig. 2d;

◂**Fig. 2** Deletion of ALG3 affects lipid metabolism in cancer cells. **a** Principal-component analysis (PCA) of metabolite profiling of vector control (Ctrl.) and ALG3-KO B16 cells. $n=6$ samples per group. **b** Heat-map and hierarchical cluster analysis of the upregulated and downregulated metabolites in ALG3-KO B16 cells by comparison with those of vector control. $n=6$ samples per group. **c** KEGG pathway analysis of metabolites upregulated in ALG3-KO B16 cells. **d** mRNA expression of lipid metabolism related genes in Ctrl. and ALG3-KO B16 cells. **e** IHC showed dark brown positive staining for SREBP1 and Ki67 in Ctrl. and ALG3-KO B16 tumors on 11 days after inoculation. Scale bars = 200 μm. **f** Quantitative analysis of Immunohistochemical staining of **e**. Data were collected from 5 random fields of for each of the 5 tumor samples and present ± SEM. Tumor growth curve (**g**) and host mice survival (**h**) of ALG3-KO or SREBP1-ALG3 DKO B16 cancer cells in C57BL/6 mice. Error bars represent mean ± SEM. $n=5$ tumors per group. **i** Western blot analysis of SREBP1 in control cells and ALG3-KO 786-O cells treated with 1 μM TUDCA for 24 h. **j** Quantification analysis of **i**. **k** Western blot analysis of SREBP1 in 786-O cells treated with 1 μg/ml Tunicamycin (TM) or 1 μM TUDCA for 24 h. **l** Quantification analysis of **k**. Quantification data as means ± SEM, p values by unpaired two-sided t test in **d**, **f** and two-way ANOVA in **g** and log-rank test in **h**. $^{*}p<0.05$, $^{**}p\leq0.01$, $^{***}p\leq0.001$. Data are representative of at least two to three independent experiments

Supplementary Fig. 2e). Western blotting analysis also showed the increase of SREBP1 in ALG3-deficient cancer cells (Supplementary Fig. 2f, g) and tunicamycin-treated cells (Supplementary Fig. 2h, i). We further confirmed the expression of SREBP1 in tumor tissue by immunohistochemistry staining. The immunohistochemistry staining for cell proliferation marker Ki67 revealed that B16 vector control tumors were more aggressive than ALG3-deficient B16 tumors (Fig. 2e, low panel; Fig. 2f, right panel). Compared with B16 vector control tumors, ALG3-deficient B16 tumors were characterized with higher levels of SREBP1expression (Fig. 2e, top panel; Fig. 2f, left panel). Our results indicated that inhibiting N-linked glycosylation key factor ALG3 activity significantly accumulated SREBP1 in cancer cells to affect cellular fatty acid metabolism.

Next, we tried to investigate the role of SREBP1 inhibition in ALG3-competent and ALG3-deficient cancer cells. Inhibiting SREBP1 activity by using PF-429242 dihydrochloride, a competitive inhibitor of SREBP site 1 protease [26], significantly reduced the expression of key genes involved in fatty acid synthesis both in ALG3-competent cells and ALG3-deficient cells (Supplementary Fig. 2j). Similarly, knocking down SREBP1 expression in ALG3-deficient cells (Supplementary Fig. 2k, l) also significantly decreased the expression of fatty acid synthesis related genes (Supplementary Fig. 2m). Knocking down SREBP1 in ALG3-deficient cancer cells significantly accelerated tumor growth and shortened the survival of host mice (Fig. 2g, h), which was opposite to the role of SREBP1 in ALG3-competent cancer cells of our study (Supplementary Fig. 2n, o) and previous study [27]. The opposite tumor growth role of SREBP1 in ALG3-competent and ALG3-deficient cancer cells may ascribe to the function of lipid metabolism homeostasis in cancer cells.

N-linked glycosylation of nascent proteins by the oligosaccharyltransferase plays a central role in ER homeostasis due to the use of protein-linked oligosaccharides as recognition and timing markers for glycoprotein quality control pathways [7]. Defects in the dolichol oligosaccharide assembly pathway or mutations in oligosaccharyltransferase subunits cause ER stress by the accumulation of unfolded proteins [8]. ALG3 is a mannosyltransferase in the lumen of ER to convert Man(5)GlcNAc(2)-Dol-PP to Man(6) GlcNAc(2)-Dol-PP [28]. Knocking out ALG3 dramatically decreased the N-linked glycosylation in ALG3-deficient cells (Supplementary Fig. 1j) and led to the activation of ER stress-associated proteins including XBP1, ATF4, ATF6 and EIF2a (Supplementary Fig. 2p). ER stress could promote SREBP1 activation and thus contribute to lipogenesis [29]. Tauroursodeoxycholic acid (TUDCA), a classic inhibitor of ER stress [30] significantly reduced SREBP1 expression in ALG3-deficient cells (Fig. 2i, j) as well as tunicamycin-treated cells (Fig. 2k, l). Our data demonstrated that defects of N-linked glycosylation, especially attenuated ALG3 expression in cancer cells induced ER stress to drive lipogenesis through regulating SREBP1 expression.

ALG3 depletion induces ferroptosis

Differential metabolites analyses between control and ALG3-deficient cells indicated that ALG3 deficiency significantly decreased the level of reduced glutathione (GSH) and increased the production of various unsaturated fatty acids (PUFAs, Supplementary Fig. 3a). The intracellular levels of GSH were confirmed in both mouse and human ALG3-deficient cancer cells by using GSH and GSSG assay kit (Beyotime). In consistent with the results of untargeted metabolic analyses, the intracellular levels of GSH significantly decreased in ALG3-deficient cells when compared with those in control cells (Fig. 3a, b). The PUFAs convert into reactive free radicals after reacting with the free radicals [31]. High levels of PUFAs in ALG3-deficient cells were susceptible to producing excessive reactive oxygen species (ROS, Fig. 3c, d) and led to the accumulation of malondialdehyde (MDA, Fig. 3e), which is one of the final products of polyunsaturated fatty acids peroxidation, in tumor tissues. The characteristics of cells with intercellular GSH starvation, accumulation of polyunsaturated fatty acids, ROS and MDA suggested one form of non-apoptotic cell death [32], namely, ferroptosis, occurring in ALG3-deficient cells. KEGG pathway analysis on differential metabolites also showed that ferroptosis was significantly enriched in ALG3-deficient cancer cells (Supplementary Fig. 3b). Ferroptosis is precisely regulated at multiple levels, including

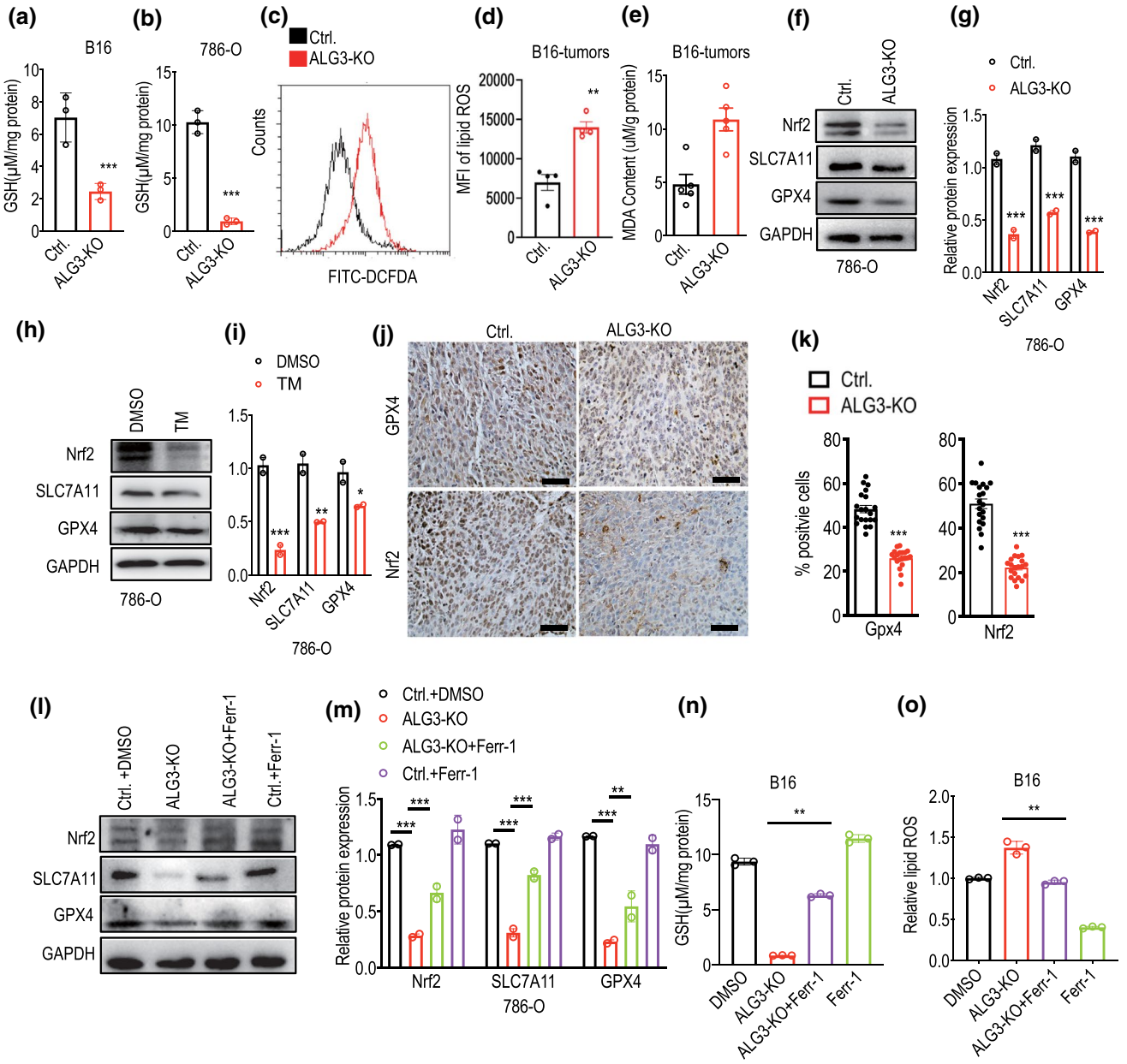

Fig. 3 ALG3 depletion induces ferroptosis. **a**, **b** ALG3 knockout significantly deceases the level of reduced glutathione (GSH) in ALG3-KO B16 (**a**) and 786-O (**b**) cells. **c**, **d** Flow-cytometry estimates ROS levels of subcutaneously grown vector control and ALG3-KO B16 tumors. **e** Level of malondialdehyde (MDA) in vector control and ALG3-KO B16 tumor tissues. **f**, **i** Western blot analysis of the expression of ferroptosis-related proteins in vector control, ALG3-KO (**f**, **g**) and Tunicamycin (TM)-treated 786-O cells (**h**, **i**). **j** IHC showed dark brown positive staining for GPX4 and Nrf2 in vector control and ALG3-KO B16 tumors on 11 days after inoculation. Scale bars = 200 μm. **k** Quantitative analysis of immunohistochemistry staining for **j**. Data were collected from 5 random fields of each of the 5 tumor samples and present mean ± SEM. *p* values were determined by unpaired two-sided *t* test. **l** Western blot analysis of the expression of ferroptosis-related proteins in ferroptosis inhibitor, ferrostatin-1 (Ferr-1)-treated ALG3-KO B16 cells. **m** Quantitative analysis of western blots for **l**. Levels of GSH (**n**) and ROS (**o**) in ferrostatin-1 (Ferr-1)-treated ALG3-KO B16 cells. Data in **a, b, d, e, g, i, k, m–o** present mean ± SEM; $n = 2$ biological replicates for **g, i, m**; $n = 3$ biological replicates for **a, b, n, o**; $n = 4$ biological replicates for **d, e**; *p* values were determined by unpaired two-sided *t* test. $^{*}p < 0.05$, $^{**}p < 0.01$, $^{***}p < 0.001$

epigenetic, transcriptional, posttranscriptional and post-translational levels [22]. Inhibiting cell membrane amino acid antiporter xCT (encoded by *SLC7A11*) reduces cystine uptake to decrease its intracellular conversion to cysteine, the rate-limiting amino acid for biosynthesis of GSH, leading to impaired function of glutathione peroxidase 4 (GPX4), and subsequent propagation of lipid peroxidation to mediate ferroptosis. Transcription factor NFE2L2 (Nrf2) plays

a central role in upregulating anti-ferroptotic defense [17]. The expression of these three key regulators of ferroptosis were examined in ALG3-deficient cancer cells and tunicamycin-treated cells. Western blotting and qRT-PCR analyses showed that both deletion of ALG3 and tunicamycin treatment significantly reduced the expression of SLC7A11, GPX4 and Nrf2 in cancer cells (Fig. 3f–i) and tumor tissues (Supplementary Fig. 3c). Furthermore, immunohistochemistry staining analysis indicated that the expression of GPX4 and Nrf2 significantly decreased in ALG3-deficient tumors (Fig. 3j, k). Moreover, a ferroptosis inhibitor, Ferrostatin-1 (Ferr-1) rescued ALG3-deficiency-mediated attenuation of SLC7A11, GPX4 and Nrf2 expression (Fig. 3l, m), and GSH content in cancer cells (Fig. 3n; Supplementary Fig. 3d). Ferrostatin-1, a lipid ROS scavenger [33], significantly decreased ROS accumulation induced by ALG3 deficiency in cancer cells (Fig. 3o; Supplementary Fig. 3e). Our data demonstrated that ALG3 depletion induced the activation of ferroptotic cell death signaling in cancer cells.

ALG3 depletion promotes intratumoral T-cell infiltration and synergizes with immunotherapy

Previous studies suggested that bursting ferroptotic cells release pro-inflammatory damage-associated molecular patterns (DAMPs) that trigger the innate immune system [34]. We first analyzed public RNA sequencing data from NCBI Gene Expression Omnibus (Accession Number: GSE128392) and evaluated correlations between ferroptosis and immune gene expression profiles [35]. Interestingly, a pro-inflammatory cytokine, interferon-gamma (IFNγ)-treated cells had lower expression levels of ALG3 as well as ferroptotic regulators (SLC3A2 and SLC7A11) when compared with control cells (Fig. 4a). Knocking out ALG3 in Renca cancer cells significantly upregulated the expression of IFNγ cytokine (Fig. 4b) and interferon-related genes (Supplementary Fig. 4a, b). IFNγ treatment activated interferon signaling pathway and stimulated MHC class I expression, antigen presentation on cells (Fig. 4a). We then examined MHC I (H-2K^d/H-2D^d) expression on the surface of ALG3-deficient Renca cells with IFNγ upregulation. Flow cytometry analysis showed that knocking out ALG3 significantly increased the MHC I (H-2K^d/H-2D^d) expression on IFNγ-upregulated ALG3-deficient Renca cells (Fig. 4c). A type I ferroptosis activator erastin, which selectively inhibits its xCT transporter, also stimulated MHC I expression in Renca cells. However, RSL3, a type II ferroptosis activator that directly inhibiting GPX4, showed no effect on MHC I expression (Fig. 4c). Our results demonstrated that ferroptotic signal SLC7A11 but not GPX4 might be involved in elevating MHC I expression on ALG3-deficient cancer cells.

We further examined the effect of ALG3 knockout on MHC I (H-2Kb/H-2D^b) expression on the surface of B16 tumor cells in vivo. Our analysis indicated that the expression of MHC I on the tumor cell surface was significantly enhanced on the surface of ALG3-deficient tumors when compared with control (Fig. 4d, e). Similarly, ALG3 deficiency also significantly increased the mRNA and protein levels of human leukocyte antigen (HLA)-A2 in the human MDA-MB-231 cancer cells (Supplementary Fig. 4c, d). These data demonstrated that ALG3 depletion increased the immunogenicity of cancer cells through ferroptotic signaling activation, pro-inflammatory signaling stimulation and MHC I upregulation.

To investigate the ability of immunogenic ALG3-deficient cells to attract lymphocyte infiltration on tumor sites, we proposed to analyze tumor infiltrating lymphocytes (TIL) in control and ALG3-deficient B16 tumors by immunofluorescence staining and flow cytometry as described previously [36]. Immunofluorescence staining indicated that ALG3 depletion caused an overall increase in intratumoral infiltration of CD45$^+$ leukocytes (Supplementary Fig. 4e, f) and CD8$^+$ T cells (Fig. 4f, g). Flow cytometry analysis confirmed the significant increase in the number of intratumoral CD8$^+$ cytotoxic T cells (CTLs) (Fig. 4h) in ALG3-deficient tumors. In addition, consistently, the number of IFNγ$^+$ and granzyme B$^+$ (GZMB$^+$) CTLs also increased significantly in ALG3-deficient tumors (Fig. 4i, j). By contrast, no significant increases in the number of CD4$^+$ Foxp3$^+$ regulatory T (Treg) cells and natural killer (NK) cells were observed in ALG3-deficient tumors when compared with vector control tumors (Supplementary Fig. 4g, h).

In order to determine the relative importance of CD8$^+$ T cells in vivo, we used a well-established antibody-based approach to deplete CD8$^+$ T cells to assess the relative importance in regulating the growth of ALG3-deficient tumors [36]. Our data indicated that depleting CD8$^+$ T cells completely abolished the growth delay of ALG3-deficient tumors (Fig. 4k, l). Furthermore, ALG3 deficiency did not influence the ability of B16 cells to form tumors in athymic nude mice which do not have mature T cells (Supplementary Fig. 4i, j).

We further determined the influence of ALG3 deficiency on CD8$^+$ T cells-mediated killing of tumor cells by using the OT-1 transgenic mouse model [37], with which we isolated and activated chicken ovalbumin (OVA)-specific CD8$^+$ T cells, presenting OVA-derived peptides (SIINFEKL). The cytotoxic effects of these T cells against OVA-transduced, IFNγ-stimulated vector control and ALG3-deficient B16 melanoma cells were evaluated in vitro. Our results indicated that IFNγ-stimulated ALG3-deficient B16 cells were significantly more susceptible than IFNγ-stimulated control cells to be killed by cytotoxic CD8$^+$ T cells (Fig. 4m, n). Consistent with our preclinical data, expression of ALG3 negatively correlated with the expression of CTL marker CD8A in various types of human malignancies (Supplementary

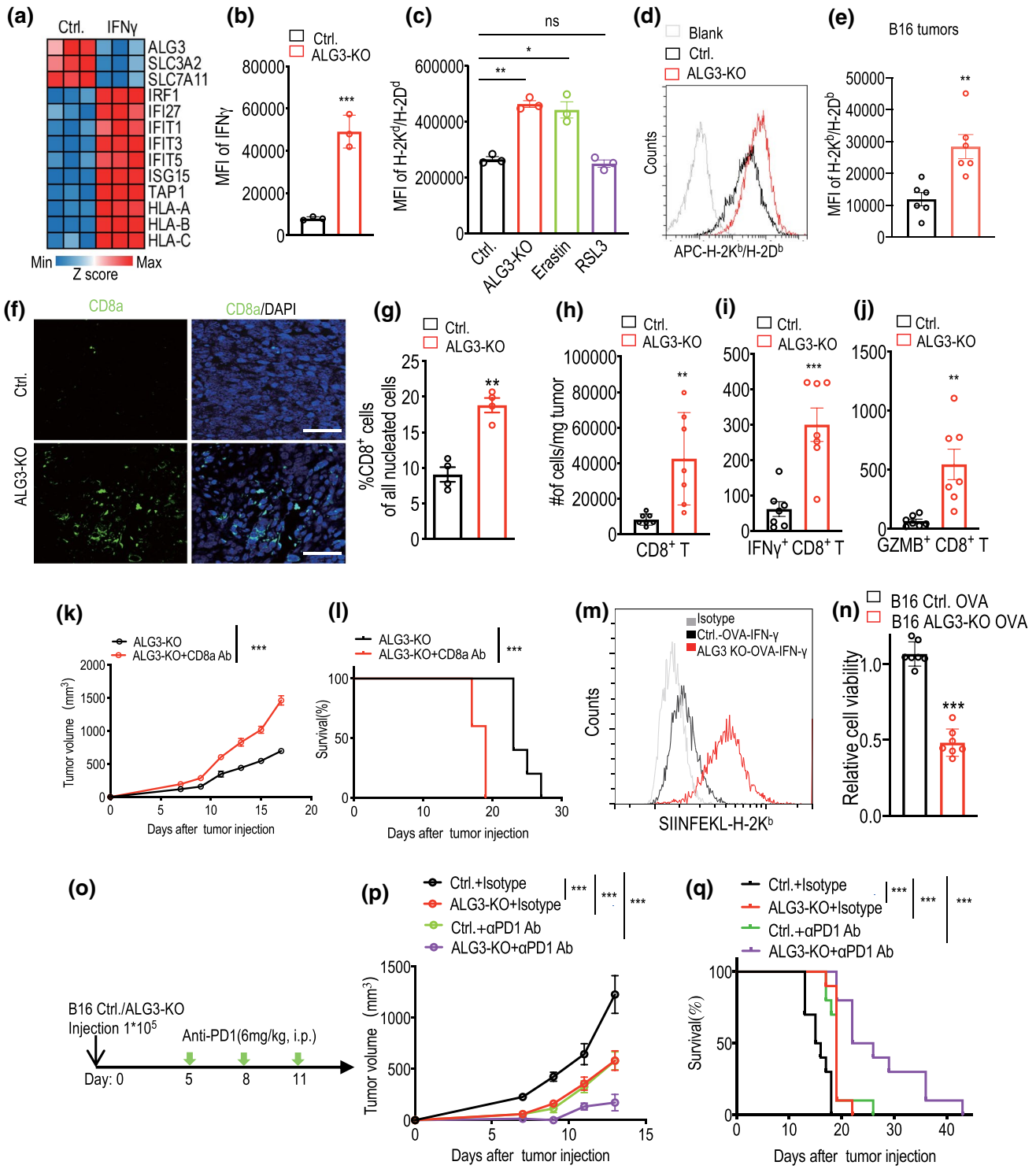

Fig. 4k). Our results demonstrated that deleting of *ALG3* gene in murine cancer cells attenuates their growth in mice in a $CD8^+$ cytotoxic T cells dependent manner.

To evaluate whether N-linked glycosylation deficiency could synergize with immune checkpoint blockade therapy, we established control and ALG3-deficient B16 tumors in C57BL/6 mice and treated with murine anti-PD1 immune checkpoint inhibitor at a dose of 6 mg/kg by intraperitoneal injection on day 5, day 8 and day 11 (Fig. 4o). Our results indicated that ALG3 deficiency synergized with anti-PD1 antibody therapy in suppressing tumor growth (Fig. 4p) and prolonging survival of host mice (Fig. 4q).

◂**Fig. 4** ALG3 depletion potentiates tumor immunogenicity and promotes pro-inflammatory tumor microenvironment. **a** Heatmap of genes expression related to ferroptosis, interferon signals, and MHC I in IFNγ-treated HT1080 cells. **b** FACS analysis of the IFNγ cytokine levels in vector control and ALG3-KO Renca cells. **c** FACS analysis of H2-K^d/H2-D^d levels on the surface of control, ALG3-KO, and ferroptosis activators (Erastin and RSL3) -treated Renca cells. **d**, **e** FACS analysis of H2-K^b/H2-D^b levels on the surface of subcutaneously growth control and ALG3-KO B16 cells on day11 after inoculation. **f** Immunofluorescence staining of CD8a in control and ALG3-KO B16 tumors on day 11 after inoculation. DAPI was used for nucleus staining. Scale bars = 50 μm. **g** Quantitative analysis of immunofluorescence staining for CD8a in **f**. Data were collected from 4 random fields of tumor samples and present mean ± SEM. *p* values were determined by unpaired two-sided *t* test. **h** Quantitative estimate the number of $CD8^+$ lymphocytes per mg of tumor tissue in control and ALG3-KO B16 tumors as determined by flow cytometry. Average numbers of tumor infiltrating IFNγ^+ $CD8^+$ (**i**) and $GZMB^+CD8^+$ (**j**) T cells per mg of tumor tissue in control and ALG3-KO B16 tumors. **k** Tumor growth of ALG3-KO B16 tumors in C57BL/6 mice depleted of $CD8^+$ T cells. $n = 5$ tumors per group. **l** Host mice survival of ALG3-KO B16 tumors in C57BL/6 mice depleted of $CD8^+$ T cells. $n = 5$ tumors per group. **m** FACS analysis of H2-K^b/H2-D^b levels on the surface of 1 ng/ml IFNγ-treated ALG3-KO-OVA and vector control B16-OVA cells. **n** Relative cell viability of control B16-OVA and ALG3-KO B16-OVA cells when co-cultured with T cell from OT-1 mouse for 48 h. Experimental protocol (**o**), tumor growth (**p**) and host mice overall survival (**q**) of ALG3-KO or vector control B16 tumors in C57BL/6 mice after treated with anti-PD1 antibody. $n = 5$ tumors per group. i.p., intraperitoneal. Data in **b, c, e, g–k, n** present mean ± SEM; $n = 3$ biological replicates for **b, c**; $n = 6$ biological replicates for **e**; $n = 7$ biological replicates for **h–j**, **n**; *p* values were determined by unpaired two-sided *t* test for **b, c, e, g–j, n**; Two-way ANOVA for **k**, **p**. $^*p < 0.05$, $^{**}p < 0.01$, $^{***}p < 0.001$

Blocking cellular N-linked glycosylation synergizes with immunotherapy

To evaluate the effect of N-linked glycosylation on immunotherapy, we analyzed the differential expressed genes (DEGs) between high G score and low G score group in KIRC patients. The volcano plot showed 604 up-regulated DEGs, in which PD1 and CTLA-4 were listed (Fig. 5a). We then performed a gene set enrichment analysis (GSEA) and found that the DEGs were significantly enriched in adaptive immune system pathway in the TCGA–KIRC patients' cohort (Fig. 5b).

Next, we examined whether pharmaceutical inhibition of N-linked glycosylation could promote intratumoral T-cell infiltration. Flow cytometry analysis showed that tunicamycin-treated cells significantly increased the MHC I (H-2K^d/H-2D^d) expression in Renca cells (Fig. 5c). Similarly, tunicamycin treatment also significantly increased human leukocyte antigen (HLA)-A2 in the human 786-O cancer cells (Fig. 5d).

To investigate the effect of tunicamycin on attracting lymphocyte infiltration on tumor site, we determined the changes of intratumoral infiltrating lymphocytes in tunicamycin-treated B16 tumors. In consistent with ALG3-deficient tumors data, tunicamycin treatment significantly increased the amount of total intratumoral $CD45^+$ leukocytes (Fig. 5e), $CD8^+$ cytotoxic T cells, functional IFNγ^+ $CD8^+$ and $GZMB^+$ $CD8^+$ T cells in tumors (Fig. 5f–h), as well as intratumoral expression of CD8a and GZMB (qRT-PCR, Fig. 5i, j). In contrast, no significant increase of $CD4^+Foxp3^+$ regulatory T (Treg) (Fig. 5k), or NK cells (Fig. 5l) was detected. To evaluate whether N-linked glycosylation defect could synergize with immune checkpoint blockade therapy, we treated parental B16 tumors in C57BL/6 mice with tunicamycin and anti-PD1 immune checkpoint inhibitor as the indicated procedure. Our data showed that tunicamycin synergized with anti-PD1 antibody therapy in suppressing tumor growth (Fig. 5m) with no significant body weight loss (Fig. 5n). These data demonstrated that blocking N-linked glycosylation by genetic deletion ALG3 or pharmaceutical inhibition could enhance cancer immune checkpoint blockade therapy in mice models.

ALG3 expression is associated with malignancy and prognosis in patients

To determine the relevance of ALG3 expression in human cancer malignancies, we evaluated the status of ALG3 in two cohorts of human subjects with cancer. In the first cohort, 150 tumor samples from subjects with kidney renal clear cell carcinoma (KIRC, Supplementary Fig. 5a for subject characteristics) were examined through immunohistochemical analysis (Fig. 6a). We found higher ALG3 expression in high grade KIRC (III–IV grades) when compared with lower grade KIRC (Supplementary Fig. 5a), suggesting a positively clinicopathological significance between ALG3 expression and tumor malignancy.

Consistent with our results in mice (Fig. 1), subjects with high amounts of ALG3 in their tumor samples showed a significantly worse overall survival (Fig. 6b). In the second cohort, 37 subjects with advanced stage colon adenocarcinoma (COAD, Supplementary Fig. 5b for subject characteristics) were analyzed through immunohistochemical analysis (Fig. 6c). Subjects with strong ALG3 staining had significantly shorter survival times (Fig. 6d). In addition, we analyzed the public RNA sequencing data from TCGA data sets (Table S4). Consistent with the immunohistochemical analysis of the two cohorts, high *ALG3* mRNA level was correlated with significantly poorer overall survival of patients with KIRC (Fig. 6e), COAD (Fig. 6f), LIHC (Fig. 6g), LUAD (Fig. 6h), PACA (Fig. 6i) and SKCM (Fig. 6j) in TCGA database. On the basis of our results, we conclude that evaluated tumor ALG3 level predicts worse overall survival in subjects with cancer, and ALG3 may serve as a predictive marker for the prognoses of the patients with malignancies.

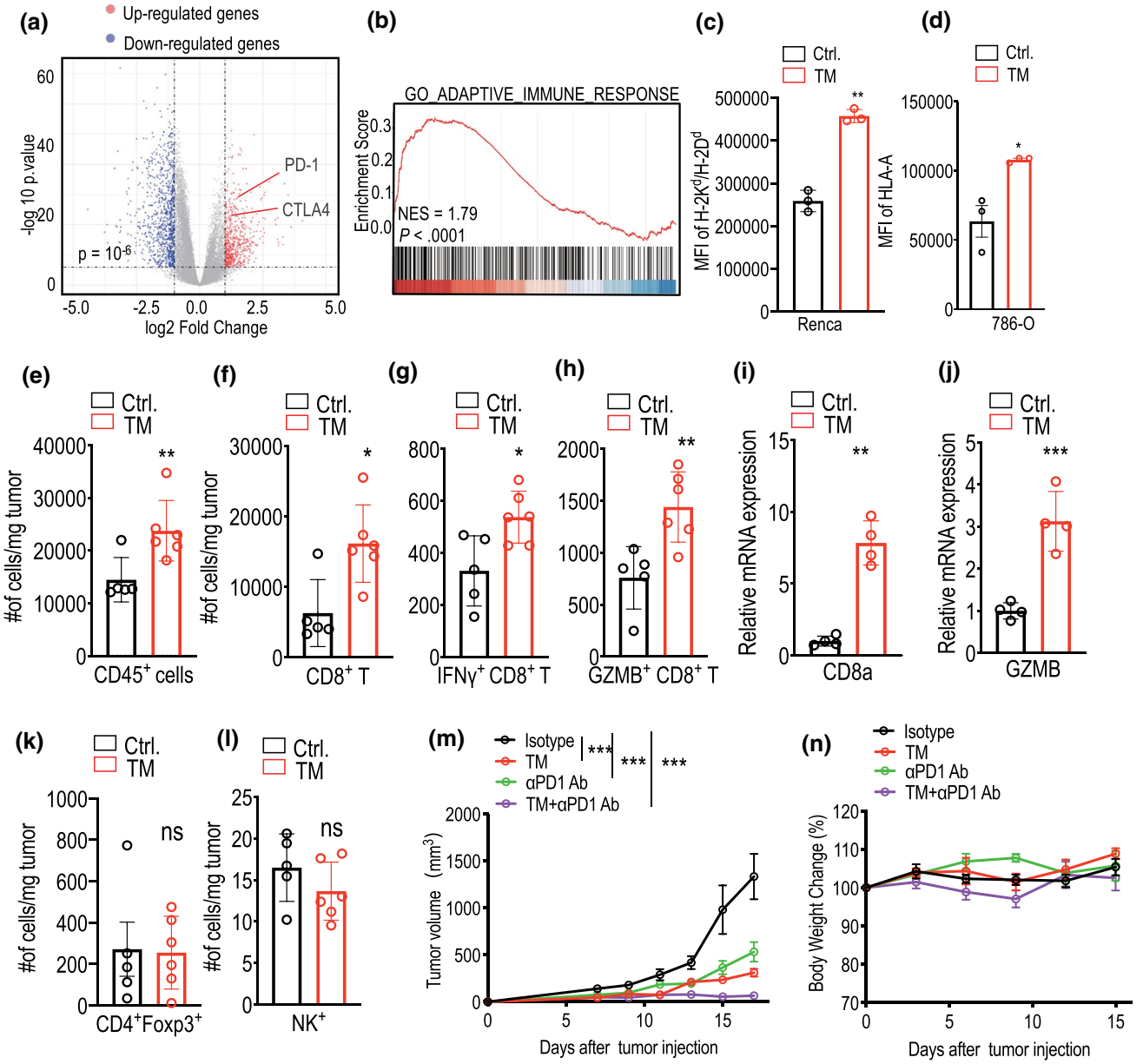

Fig. 5 N-linked glycosylation inhibitor Tunicamycin synergized with immune checkpoint blockade therapy. **a** Volcano plot showed the 604 up-regulated and 966 down-regulated differential expressed genes (DEGs) between the high and low G score in the TCGA-KIRC cohort. (|log2Foldchange| ≥ 1 and p value < 10^{-6}). **b** Gene set enrichment analysis (GSEA) discovered the DEGs between high G score and low G score of patients in the TCGA-KIRC cohort were enriched in adaptive immune system pathway. **c** FACS analysis of H2-K^d/H2-D^d levels on the surface of subcutaneously growth control and ALG3-KO Renca cells. **d** FACS analysis of HLA-A2 levels on the surface of subcutaneously growth control and ALG3-KO 786-O cells. **e** Average numbers of tumor infiltrating $CD45^+$ cells per mg of tumor tissue in Ctrl. and 0.1 mg/kg Tunicamycin-treated B16 tumors. Average numbers of tumor infiltrating $CD8^+$ (**f**), $IFN\gamma^+$ $CD8^+$ (**g**) and $GZMB^+CD8^+$ (**h**) T cells per mg of tumor tissue in Ctrl. and 0.1 mg/kg Tunicamycin-treated B16 tumors. **i-j** qRT-PCR data showing the expression of CD8a(i) and GZMB(j) in Ctrl. and 0.1 mg/kg Tunicamycin-treated B16 tumors. $n = 4$ for each group. Average numbers of tumor infiltrating $Foxp3^+$ $CD4^+$ T cells (**k**) and NK+ cells (**l**) per mg of tumor tissue in Ctrl. and 0.1 mg/kg Tunicamycin-treated B16 tumors. $n = 5$ for control, and $n = 6$ for Tunicamycin treatment. Tumor growth (**m**) and mice body weight (**n**) of B16 tumors bearing C57BL/6 mice treated with Tunicamycin (TM) and anti-PD1 antibody. $n = 5$, 6, 5, and 6 mice in the four groups, respectively. i.p., intraperitoneal. Data in **c–l** present mean ± SEM. p values were determined by two-way ANOVA for **m**; log-rank t test for **n**. $^*p < 0.05$, $^{**}p < 0.01$, $^{***}p < 0.001$

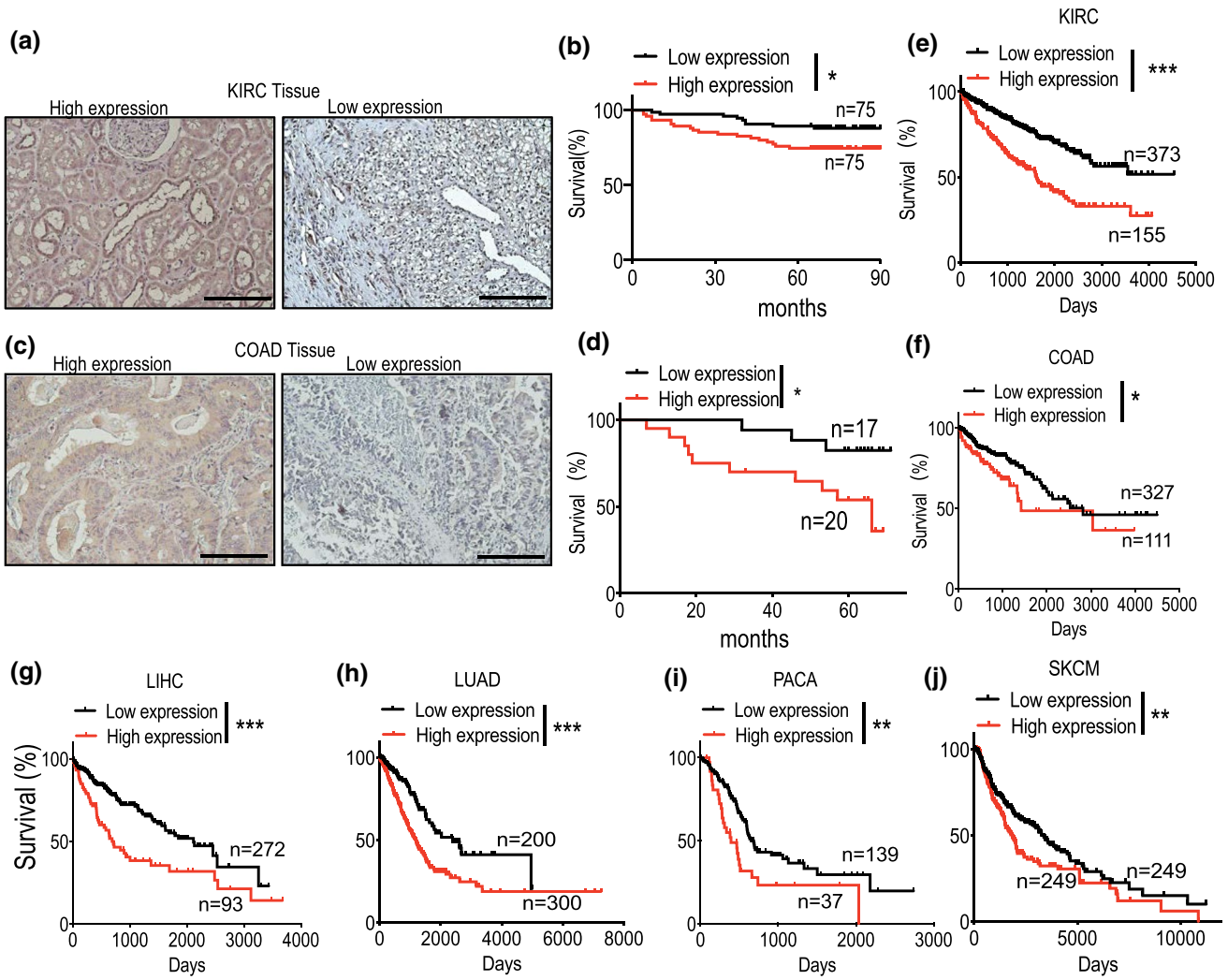

Fig. 6 High expression of ALG3 is associated with worse overall survival of patients. **a** Representative IHC staining patterns for samples with high and low expression of ALG3 in KIRC samples. Scale bars = 50 μm. **b** Kaplan–Meier survival analysis of a cohort of 150 patients with KIRC related **a**. **c** Representative IHC staining patterns for samples with high and low expression of ALG3 in COAD samples. Scale bars = 50 μm. **d** Kaplan–Meier survival analysis of a cohort of 37 patients with COAD related **c**. **e–f** Kaplan–Meier survival analysis of the relationship between cumulative survival and ALG3 mRNA expression in TCGA KIRC samples (**e**, $n = 528$), and COAD samples (**f**, $n = 438$). Data information is listed in Table S4. Higher levels of ALG3 mRNA expression correlated with worse survival in 4 cohorts of patients with cancer, including liver hepatocellular carcinoma (LIHC, **g**), lung adenocarcinoma (LUAD, **h**), pancreatic cancer (PACA, **i**) and skin cutaneous melanoma (SKCM, **j**). Detail information is listed in Table S4. Log-rank test were used to analyze the statistical significance between groups of high and low ALG3 in **b**, **d–j**. $*p < 0.05$, $***p < 0.001$

Discussion

This study uncovers an unappreciated mechanism that ALG3 inhibition or N-linked glycosylation blockade induces lipid homeostasis disorder to trigger immunogenic ferroptosis of cancer cells, thereby potentiates intratumoral cytotoxic T cell infiltration and renders tumors more responsive to immune checkpoint blockade therapy (Supplementary Fig. 6), which has great translational potential.

Previous findings have shown that pathogenic variant ALG3 was associated with ALG3-congenital disorder of glycosylation (ALG3-CDG), a rare autosomal recessive disease characterized by N-glycosylation genetic defects [28, 38]. Emerging data showed that upregulation of ALG3 can promote the proliferation, radiosensitivity, lymph node metastasis, and metabolic reprogramming of cancer cells and the upregulation of ALG3 is related with poor prognosis of breast cancer, non-small cell carcinoma, head and neck squamous carcinoma [39–42], which is consistent with our study that ALG3 is an oncoprotein associated with multiple malignancies (Fig. 6).

Knocking out ALG3-mediated N-linked glycosylation defects in cancer cells promotes transcription factor SREBP1 activation and excessive lipogenesis to disrupt lipid

homeostasis through ER-stress-response modules. Although the crosstalk between N-linked glycosylation and lipid metabolism was clearly demonstrated in the study, mechanisms of how the changes of glycosylation affects the function of SREBP1 and other transcription factors need to be further explored.

Upregulation of SREBP1 caused major changes in lipid composition characterized by promotion of poly-unsaturated lipids and accumulation of ROS, subsequently leading to lipid peroxidation-related ferroptosis in cancer cells. These ferroptotic cancer cells were characterized with activation of interferon-related signal, releasing of IFNγ cytokine, and upregulating of MHC I (H-2Kb/H-2D^{b}, H-2K^{d}/H-2D^{d} and HLA-A). Furthermore, excessive accumulation of misfolded proteins might trigger neoantigens in N-linked glycosylation defects cancer cells. ALG3 inhibition may also result in exposing neoantigens continuously to make the ferroptotic cancer cells more immunogenic, subsequently activating anti-tumor immune responses. On the other hand, ferroptotic cancer cells also influence immune cells by releasing lipid metabolites, cytokines and chemokines [43], which enhance cytotoxic T cell infiltration and actively promote a pro-inflammatory microenvironment to activate anti-tumor immune responses potentiate anti-PD1 therapy. Therefore, ALG3 might be a promising target for cancer immune checkpoint blockade therapy. Although few literatures demonstrate the anti-tumor immune effect of N-linked glycosylation defects at whole cellular level, several reports have shown that inhibition of individual protein N-linked glycosylation could enhance anti-tumor T-cell immunity. For example, in a recent study the removal of N-linked glycosylation improved anti-PD-L1 antibody binding affinity and signal intensity and predicted anti-PD-1/PD-L1 therapeutic efficacy [44]. Furthermore, it has been previously shown that blocking the inhibitory signal of PD-L1 by metformin-induced abnormal PD-L1 glycosylation enhances cytotoxic T lymphocyte activity against cancer cells [45], while N-linked glycosylation of PD-L1 enhances stabilization and suppresses T-cell activity [46].

In our study, besides using multiple mouse models to demonstrate the function of ALG3 in immune regulation, we also analyzed the expression of CD8A and ALG3 in TCGA cohorts and tumor tissues of patients, which provide a good rationale for predicting the prognosis of patients with malignancies. However, further clinic-related experiments need to be carried out to confirm the translational potential of targeting ALG3 as a new strategy for cancer immune checkpoint blockade therapy.

Methods

Cell culture

MC38 mouse colon adenocarcinoma cell line was obtained from Kerafast (Boston, MA). Renca (murine renal adenocarcinoma), B16/F10 (murine melonoma), 4T1 (murine mammary carcinoma), 786-O (human renal cell carcinoma) and MDA-MB-231 (human mammary adenocarcinoma) cancer cell lines were obtained from Cell Culture Facility of Chinese Academy of Science or Guangzhou Cellcook Biotech Co. Ltd. Renca, 786-O and MDA-MB-231 cells were cultured in RMP-1640 (Gibco) supplemented with 10% fetal bovine serum (FBS), 100 unites/ml penicillin and 100 µg/ml streptomycin antibiotics, and B16/F10, 4T1, MC38, 293 T were cultured in DMEM(Gibco) supplemented with 10% fetal bovine serum (FBS), 100 unites/ml penicillin and 100 µg/ml streptomycin antibiotics. Cells were maintained at 37 °C in a humidified 5% CO_2 incubator. All cell lines were authenticated using short-tandem repeat (STR) profiling and verified to be free of mycoplasma contamination.

"G score" computation and TCGA analysis

Univariate Cox regression analysis were performed by the R package 'survival' to screen out the genes associated with prognosis. $p < 0.05$ in univariate Cox regression analysis were considered statistically significant. The prognostic gene signature was constructed by weighting the Cox regression coefficients to calculate a risk score (*G*-score) for each patient. The *G*-score was calculated as follows:

$$G\text{ - score} = \sum_{i=1}^{n} \beta_i x_i.$$

where β_i is the coeff (coefficient) and x_i is the FPKM value of each selected gene, while $Z = (\text{coeff/se(coeff)})$. The R packages 'survival' and 'survminer' were used to determine the optimal cut-off value of risk score to divide patients into high- or low-risk groups. The heatmap was generated from a cluster analysis of the normalized read counts (scaling in a per gene basis using the *z*-score ($(x-\mu)/\sigma$), Euclidean-distance, average-linkage) using the R package (v 1.0.12) 'pheatmap' (v 3.4; https://CRAN.R-project.org/package=pheatmap).

In addition, RNA-Seq data for KIRC, SKCM, LIHC, and LGG were downloaded and pre-processed with the GDC (Genomic Data Commons) query of the TCGA biolinks Bioconductor/R packages.

Differential gene expression and gene set enrichment analysis

R package "limma" was used to identify the differential expressed genes (DEGs) between high and low G score patients in TCHA–KIRC cohort. (|log2Foldchange| ≥ 1 and p value $< 1 \times 10^{-6}$ were considered as the cutoff values to identify DEGs. Then we investigate the underlying association between G score and immune-associated pathways. Gene set enrichment analysis (GSEA) was conducted between high and low G score patients in TCGA-KIRC cohort. $p < 0.05$ was considered statistically significant.

CRISPR mediated gene deletion in tumor cells

Knockout cells were generated with lentivirus-mediated CRISPR–Cas9 technology. Single guided RNA (sgRNA) sequences were designed using a public-domain online CRISPR design tool (chopchop.cbu.uib.no). SgRNA sequences targeting mouse ALG3 were as follows: sgRNA1, AAGAAGGAATAGCAATCCCG; sgRNA2, CCATAGGGA TATCAGTGCCC. SgRNA sequences targeting human ALG3 were: sgRNA1, TTCCTGCTGGAGAACCCCAG; sgRNA 2, GAGAAGAAACAGTAACCCAG. Sequences targeting mouse SREBP1 were: sgRNA 1, AATGCCCCA GCCGAAAAGCG; sgRNA 2, TTTGACGCCCCCTATGCT GG. Sequences targeting human SREBP1 were: sgRNA 1, TCTCCGCATCTACGACCAGT; sgRNA 2, CAGAAAGCG AATGTAGTCGA. Double-stranded oligonucleotides encoding the sgRNA sequences were cloned into BsmB1 (Thermal Fisher Scientific)-digested plasmid LentiCRISPRv2 (deposited by F. Zhang of MIT to Addgene, Cambridge, MA) which co-expresses Cas9 and sgRNA in the same vector. The sgRNA-encoding CRISPR lentivirus vectors were then produced using an established protocol from the Trono laboratory (https://www.epfl.ch/labs/tronolab/laboratory-of-virology-and-genetics/ lentivectors-toolbox/). To generate the knockout cell lines, target cells were infected with sgRNA-encoding CRISPR lentivirus and cultured in DMEM with 10% FBS and selected in puromycin (1 μg/ml for B16F10 and MDA-MB-23 l and Renca cells, 1.5 μg/ml for 786-O cells, 5 μg/ml for 4T1 cells and 6 μg/ml for MC38 cells) for 7–10 days.

Implantation of tumor cells, tumor growth measurements and survival analyses

Animal experiments conducted in this study were approved by Sun Yat-sen University Institutional Animal Use and Care Committee. C57BL/6, and athymic nude mice were from Sun Yat-sen University animal facility. Mice were housed in an environmentally controlled room (temperature 23 ± 2 °C, relative humidity 30–70%), fed irradiated laboratory rodent diet, and provided with sterilized water. Before tumor cells were injected, age-matched 6–8-week-old mice were shaved at the flank. Tumor cells were then injected into the shaved flank subcutaneously, using 1×10^5 CRISPR–Cas9-modified control or ALG3-knockout tumor cells. Anti-PD1 antibody (Clone RMP1-14, BioXcell) were intraperitoneally (i.p.) administrated at dose of 6 mg/kg on day 5, day 8 and day 11 in combination with ALG3 deficiency or Tunicamycin. Tunicamycin (MedChemExpress, MCE, Shanghai) was intraperitoneally (i.p.) administrated at dose of 0.1 mg/kg/day (in water) for consecutive 8 days starting on day 3 after tumor inoculation. No blinding was used in our tumor growth delay experiments. Tumor size were measured by use of a caliper and calculated using the formula volume = (length)(width)^2/2. Endpoint was defined as the time when a progressively growing tumor reached 15 mm in the longest dimension. Tumor samples were collected at the indicated times and processed for bioanalysis.

Cell viability assay

Cancer cells were plated at 2000 per well in 96-well flatted bottom white cell culture plates (Corning). Growth viability was determined by CCK8(MCE). A total of 10 μl of CCK8 working solution was added to each well at 0, 24, 48, or 72 h followed by incubation for 2 h at 37 °C. Finally, the absorbance was measured at 450 nm.

Western blot analysis

Cells were washed with cold phosphate-buffered saline (PBS), then lysed in radioimmunoprecipitation assay (RIPA) buffer supplemented with protease inhibitors (Sigma). Equal amounts of lysates were separated by SDS-PAGE and transferred to polyvinyldifluoride (PVDF) membrane. Proteins were then probed with specific antibodies followed by secondary antibodies conjugated with horseradish peroxidase (HRP). The HRP signal was developed by electrochemiluminescence (ECL). For glycosyaltion detection. The cell lysates were normalized for total protein using a Bradford assay and then separated by SDS-PAGE. proteins were transferred to PVDF membranes. Membranes were incubated for 1 h in Tris-buffered saline containing 0.1% Tween-20 and 2% BSA and then probed overnight with biotin conjugates of concanavalin A (ConA-biotin; C2271; Sigma). After 1 h incubation with streptavidin-peroxidase (S5512; Sigma), the blots were visualized using ECL. Quantification of interested proteins was analyzed using Image J.

Quantitative real-time PCR (qRT-PCR) assay

Total RNA was extracted using TRIzol Reagent (Invitrogen) according to the manufacturer's protocol. The RNA

was subjected to cDNA synthesis with random hexamer primers using Superscript II reverse transcriptase (Invitrogen). Real-time quantitative RT-PCR (qRT-PCR) was performed SYBR PrimeScript RT-PCR kit (TaKaRa Bio Inc, Japan). The primer sequences are as follows: *HLA-A* forward primer: 5′-accctcgtcctgctactctc-3′, reverse primer: 5′-ctgtctcctcgtcccaatact-3′; *SCAP* forward primer: 5′-tatctcgggccttctacaacc-3′, reverse primer: 5′-ggggcgagtaatccttcaca-3′; *FASN* forward primer: 5′-aaggacctgtctaggtttgatgc-3′, reverse primer: 5′-tggcttcataggtgacttcca; *SREBP1* forward primer: 5′-acagtgacttccctggcctat-3′, reverse primer: 5′-gcatggacgggtacatcttcaa-3′; *ERLIN2* forward primer: 5′-tccaccacgaactgaaccag-3′, reverse primer: 5′-aacagctcaatgtagacctcttg; *ACAT2* forward primer: 5′-gcggaccatcataggttcctt-3′, reverse primer: 5′-actggcttgtctaacaggattct-3′; human-*GAPDH* forward primer: 5′-gggaaactgtggcgtgat-3′, reverse primer: 5′-gagtgggtgtcgctgttga-3′; mouse-*H2-K1* forward primer: 5′-gcacaggttcgcgttcgaga-3′, reverse primer: 5′-ctggatttgccaggagttcgg-3′; mouse-*FASN* forward primer: 5′-ggaggtggtgatagccggtat-3′, reverse primer: 5′-tgggtaatccatagagcccag-3′; mouse-*GPX4* forward primer: 5′-tgtgcatcccgcgatgatt-3′, reverse primer: 5′-ccctgtacttatccaggcaga-3′; mouse-*TAP1* forward primer: 5′-ggacttgccttgttccgagag-3′, reverse primer: 5′-cagcatccgacacagcatgt-3′; mouse-*XBP1* forward primer: 5′-agcttttacgggagaaaactcac-3′, reverse primer: 5′-cctctggaacctcgtcagga-3′; mouse-*ATF4* forward primer: 5′-cctgaacagcgaagtgttgg-3′, reverse primer: 5′-tggagaacccatgaggtttcaa-3′; mouse-*ATF6* forward primer: 5′-tcgcctttagtccggttctt-3′, reverse primer: 5′-ggctccataggtctgactcc-3′; mouse-*EIF2A* forward primer: 5′-cacggtgcttcccagagaatc-3′, reverse primer: 5′-gtcccttgttagcgacattga-3′; mouse-*ERLIN2* forward primer: 5′-atctcatgctcccgttcatca-3′, reverse primer: 5′-cactgcatttgggaccagga-3′; mouse-*IFIT1* forward primer: 5′-ctgagatgtcacttcacatggaa-3′, reverse primer: 5′-gtgcatcccaatgggttct-3′; mouse-*ISG15* forward primer: 5′-ctagagctagagcctgcag-3′, reverse primer: 5′-agttagtcacggacaccag-3′; mouse-*SCAP* forward primer: 5′-ccgagcattccaactggtg-3′, reverse primer: 5′-ccatgttcgggaagtaggct-3′; mouse-*GAPDH* forward primer: 5′-ggcctccaaggagtaagaaa-3′, reverse primer: 5′-gcccctcctgttattatgg-3′.

Global metabolomics analysis by LC–MS/MS

Metabolite extraction was primarily performed according to previously reported methods [47, 48]. In brief, 100 µl samples were extracted by directly adding 300 µl of precooled methanol and acetonitrile (2:1, v/v), internal standards mix 1 (IS1) and internal standards mix 2 (IS2) were added for quality control of sample preparation. After vortex for 1 min and incubate at − 20 °C for 2 h, samples were centrifuged for 20 min at 4000 rpm, and the supernatant was then transferred for vacuum freeze drying. The metabolites were resuspended in 150 µl of 50% methanol and centrifuged for 30 min at 4000 rpm, and the supernatants were transferred to autosampler vials for LC–MS analysis. A quality control (QC) sample was prepared by pooling the same volume of each sample to evaluate the reproducibility of the whole LC–MS analysis.

The samples were analyzed on a Waters 2D UPLC (Waters, USA), coupled to a Q-Exactive mass spectrometer (Thermo Fisher Scientific, USA) with a heated electrospray ionization (HESI) source and controlled by the Xcalibur 2.3 software program (Thermo Fisher Scientific, Waltham, MA, USA). Chromatographic separation was performed on a Waters ACQUITY UPLC BEH C18 column (1.7 µm, 2.1 mm × 100 mm, Waters, USA), and the column temperature was maintained at 45 °C. The mobile phase consisted of 0.1% formic acid (A) and acetonitrile (B) in the positive mode, and in the negative mode, the mobile phase consisted of 10 mM ammonium formate (A) and acetonitrile (B). The gradient conditions were as follows: 0–1 min, 2% B; 1–9 min, 2–98% B; 9–12 min, 98% B; 12–12.1 min, 98% B to 2% B; and 12.1–15 min, 2% B. The flow rate was 0.35 ml/min and the injection volume was 5 µl. The mass spectrometric settings for positive/negative ionization modes were as follows: spray voltage, 3.8/− 3.2 kV; sheath gas flow rate, 40 arbitrary units (arb); aux gas flow rate, 10 arb; aux gas heater temperature, 350 °C; capillary temperature, 320 °C. The full scan range was 70–1050 m/z with a resolution of 70,000, and the automatic gain control (AGC) target for MS acquisitions was set to 3×10^6 with a maximum ion injection time of 100 ms. Top 3 precursors were selected for subsequent MSMS fragmentation with a maximum ion injection time of 50 ms and resolution of 17,500, the AGC was 1×10^5. The stepped normalized collision energy was set to 20, 40 and 60 eV.

ROS detection

ROS production was detected using the probes DCFDA (Abcam, ab113851). 5×10^5 cells were harvested, washed with PBS, and incubated with 20 µM DCFDA for 30 min at 37 °C. The samples were analyzed using flow cytometer Cytoflex (Beckman). Analysis of flow cytometry data was performed with FlowJo v10. The relative lipid ROS were calculated by the ratio of mean fluorescence intensities (MFI) of FITC.

Malondialdehyde (MDA) assay

MDA content in tumor cells or tissue was measured by Lipid Peroxidation MDA Assay Kit (Beyotime) to monitor the lipid peroxidation. Cultured cells or tumor tissue was lysed and homogenized in RIPA buffer containing protease inhibitors. Tissue homogenates were centrifuged at 1600×*g* for 10 min at 4 °C and 100 µl supernatant was used for MDA

analysis. In the meantime, protein concentration of supernatant was determined by bicinchoninic acid (BCA) protein assay for quantification of MDA content.

Immunofluorescence staining and immunohistochemistry (IHC) assay

Tumor tissues were fixed, embedded into paraffin and sectioned in standard procedure. After antigen retrieval and blocking, the sections were incubated with the anti-mouse CD45 antibody in blocking buffer at 4 °C overnight, sequentially stained with FITC-conjugated rat anti-mouse secondary antibody for 1 h at room temperature. After washing with PBS, the stained slices were mounted with mounting medium (Vector Laboratories) containing DAPI. Images were captured by use of Leica SP-5 confocal microscope. For IHC assay, tumor sections were incubated with primary and HRP-conjugated secondary antibody, then visualized with HRP/DAB system. Images were captured with light microscope (Olympus, BX43) and counted with Image-Pro Plus software (Media Cybernetics, IncRockville, MD). The primary antibodies used for IHC are listed as follows. Mouse anti-SREBP1 Monoclonal antibody (1:500, Cat No. 66875-1, Proteintech Inc), rabbit anti-Ki67 polyclonal antibody (1:500, Cat No. 27309-1, Proteintech Inc), anti-rabbit Nrf2 monoclonal antibody (1:200, Cat No. 16396-1, Proteintech Inc), or rabbit anti-GPX4 polyclonal antibody (1:200, Cat No. 14432-1, Proteintech Inc).

For staining ALG3 in human tumor tissues, human KIRC tissue microarray was approved by the Ethical Review Board of Shanghai Outdo Biotech Company (No. SHYJS-CP-1510001).

Human COAD tissue microarray was approved by the Ethical Review Board of Shanghai General Hospital, Shanghai Jiao Tong University School of Medicine, China (no. 2014KY107).

Assessment of GSH levels

The intracellular levels of GSH were measured using GSH and GSSG Assay Kit (Beyotime). According to the manufacturer's instructions, the IsoA-treated cells were collected and homogenized. The protein concentrations were quantified using the BCA method. The total GSH levels were carefully measured by the enzymatic recycling method using glutathione reductase and 5′,5′-dithio-bis (2-nitrobenzoic acid). The sulfhydryl group of GSH reacts with DTNB and produces a yellow-colored 5-thio-2-nitrobenzoic acid, which has an absorbance at 405 to 414 nm. Oxidized glutathione (GSSG) levels were accomplished first by first derivatizing GSH with 2-vinylpyridine. The concentrations of reduced GSH were calculated by subtracting the GSSG levels from the total GSH (GSH = total GSH − 2 × GSSG). The intracellular levels of GSH were determined on the basis of cellular protein concentrations.

Analyses of tumor infiltrating lymphocytes and MHC I on tumor cells

About 1×10^5 Ctrl. or ALG3-KO tumor cells were inoculated subcutaneously into C57BL/6 mice. Tumors were harvested on day 12 after inoculation, weighted, mechanically minced and incubated with 50 μg/ml DNase I (Sigma) and 2 mg/ml collagenase P (Sigma) for 20 min at 37 °C. The dissociated cells were filtered, blocked with an anti-CD16/32 antibody and stained with indicated surface antibodies for 20 min on ice. Dead cells were marked by use of Live/Dead Fixable Violet dye (Thermo Fisher). Intracellular antibodies were added after fixation and permeabilization following the manufacturer's instructions (Biolegend). For MHC I detection in vivo, B16 with GFP stabilizing expression cells were inoculated into C57BL/6 mice and treated with the same procedure. Tumor cells were identified with GFP and stained with anti-H-2Kb/H-2D^b antibody. The samples were analyzed and quantified using flow cytometer Cytoflex (Beckman). The list of antibodies, their source, and dilution information are as follows. FITC anti-Mouse CD45(Clone 30-F11, Cat No. #103108, 0.25 μg per 10e6 cells in 100 μl dilution buffer, Biolegend). PE/Cyanine7 anti-Mouse CD3ε (Clone 145-2c11, Cat No. #100320, 1 μg per 10e6 cells in 100 μl dilution buffer, Biolegend). Alexa Fluro 647 anti-Mouse CD4 (Clone GK1.5, Cat No. #100424, 0.25 μg per 10e6 cells in 100 μl dilution buffer, Biolegend). APC/Fire750 anti-Mouse CD8a (Clone 53–6.7, Cat No. #100766, 0.25 μg per 10e6 cells in 100 μl dilution buffer, Biolegend). PE anti-Mouse NK1.1(Clone PK136, Cat No. #108707, 0.25 μg per 10e6 cells in 100 μl dilution buffer, Biolegend). PE anti-Mouse Foxp3 (Clone MF-14, Cat No. #126403, 1 μg per 10e6 cells in 100 μl dilution buffer, Biolegend). PE anti-Mouse Gzmb (Clone QA16A02, Cat No. #372207, 5 μl per 10e6 cells in 100 μl dilution buffer, Biolegend). Alexa Fluro 647 anti-Mouse IFNγ (Clone XMG1.2, Cat No. #505816, 0.25 μg per 10e6 cells in 100 μl dilution buffer, Biolegend). APC anti-Mouse H-2Kb/D^b (Clone 28–8-6, Cat No. #114614, 0.25 μg per 10^6 cells in 100 μl dilution buffer, Biolegend). Purified anti-Mouse CD45 (Clone 30-F11, Cat No. #103101, IF, 1:50 dilution, Biolegend).

CD8$^+$ lymphocyte depletion

To evaluate the role of specific subsets of immune effector cells in mice, we depleted CD8$^+$ T cells using 100 μg of anti-CD8β antibody (BioXcell, clone 53–5.8), respectively, on day − 3, day 0 and day 3. Equal amounts of IgG isotype antibodies (BioXcell) were injected as a control.

OT-1 T cell culture

OT-1 $CD8^+$ T cells expressing a transgene encoding a TCR that specifically recognizes SIINFEKL peptide bound to mouse H-2Kb were harvested from spleens of OT-1 C57BL/6 mice. Activated OT-1 T cells were generated by incubating 5×10^6 OT-1 SIINFEKL-pulsed mouse splenocytes per millilitre in vitro for 5–7 days in the presence of mouse recombinant interleukin-2. Briefly, an OT-1 mouse spleen was harvested and homogenized using aseptic techniques. The released cells were pelleted and resuspended in 3 ml of ACK buffer (0.15 M NH_4Cl, 1 mM $KHCO_3$ and 0.1 mM EDTA) for 2 min to lyse red blood cells at room temperature. The splenocytes were then pelleted, washed, and resuspended at 5×10^6 cells per millilitre in complete growth medium (RPMI1640 Sigma-Aldrich) with 10% FBS (Corning), 1 × penicillin–streptomycin (ThermoFisher Scientific), 1 × sodium pyruvate (ThermoFisher Scientific), and 1 × 2-mercaptoethanol (ThermoFisher Scientific) containing 0.75 μg/ml SIINFEKL peptide (GenScript) and incubated at 37 °C in a 95% air/5% CO2 humidified environment. Mouse recombinant interleukin-2 (Multi Sciences) was added on days 3 and 5 at 30 U/ml with fresh complete growth medium. On day 7, the cells were harvested for assays. The specificity was determined by flow-cytometry analysis using APC/Fire750-labelled anti-mouse CD8 antibody (BioLegend).

Tumor cell/T-cell co-culture analysis

B16 control, B16 ALG3-knockout, B16 control-OVA (expressing ovalbumin) and B16 ALG3-knockout-OVA cells were first stimulated by incubation with mouse recombinant IFN-γ at 1 ng/ml for 12 h. The stimulated tumor cells were then cultured with OVA-specific T cells at a 1:1 ratio or without OVA-specific T cells in T-cell complete growth medium with mouse recombinant interleukin-2 (30 U/ml) for 24 h. Subsequently, Growth viability was determined by CellTiter-Glo luminescent viability assay (Promega).

Statistical analysis

Statistical analysis was performed using GraphPad Prism 8 software; *P* values of less than 0.05 were considered statistically significant. Two-way ANOVA was used for multiple comparisons in tumor growth delay experiments. Log-rank tests were used for mouse survival analyses. ALG3 gene expression data in Table S3 was from TCGA data sets included in cBioportal (https://www.cbioportal.org/) in February 2021 and GTEx Portal (https://www.gtexportal.org). ALG3 gene expression and patient survival data in Table S4 were from proteinatlas.org (version 20.1.) and oncolnc (http://www.oncolnc.org). Overall survivals of ALG3 high and low groups were evaluated using log-rank tests. In other experiments, comparisons between two groups were made with unpaired two-sided Student's t tests.

Supplementary Information The online version contains supplementary material available at https://doi.org/10.1007/s00018-022-04365-4.

Author contributions Conception and design: XL, CL. Development of methodology: PL, CL, JC, QH, J-AP. Acquisition of data: PL, CL, ZL, CZ, DX, ZL, LH. Writing, review, and/or revision of the manuscript: XL, PL. Study supervision: XL.

Funding This work was supported by Guangdong Basic and Applied Basic Research Foundation Grant (2020B1515020054), and Shenzhen Science and Technology Program Grant (JCY20190807154813511).

Availability of data and materials The data sets generated correlations between ferroptosis and immune gene expression profile during the current study are available in the public RNA sequencing data from NCBI Gene Expression Omnibus (accession number: GSE128392) All other data generated or analyzed during this study are included in this published article and its supplementary information files.

Declarations

Conflict of interest The authors declare no competing interests.

Ethical approval All animal experiment protocols were approved by the Sun Yat-sen University Institutional Animal Use and Care Committee.

Consent for publication All authors provided their consent to publish the study.

References

1. Pinho SS, Reis CA (2015) Glycosylation in cancer: mechanisms and clinical implications. Nat Rev Cancer 15(9):540–555. https://doi.org/10.1038/nrc3982
2. Clerc F, Reiding KR, Jansen BC, Kammeijer GS, Bondt A, Wuhrer M (2016) Human plasma protein N-glycosylation. Glycoconj J. 33(3):309–343. https://doi.org/10.1007/s10719-015-9626-2
3. Tim C, Huffaker PWR (1983) Yeast mutants deficient in protein glycosylation. Proc Natl Acad Sci USA 80:7466–7470
4. Leto DE, Morgens DW, Zhang L et al (2019) Genome-wide CRISPR analysis identifies substrate-specific conjugation modules in ER-associated degradation. Mol Cell 73(2):377-389 e11. https://doi.org/10.1016/j.molcel.2018.11.015
5. Liu K, Tan S, Jin W et al (2020) N-glycosylation of PD-1 promotes binding of camrelizumab. EMBO Rep 21(12):e51444. https://doi.org/10.15252/embr.202051444
6. Krishnan V, Bane SM, Kawle PD, Naresh KN, Kalraiya RD (2005) Altered melanoma cell surface glycosylation mediates organ specific adhesion and metastasis via lectin receptors on the lung vascular endothelium. Clin Exp Metastasis 22(1):11–24. https://doi.org/10.1007/s10585-005-2036-2
7. Bettigole SE, Glimcher LH (2015) Endoplasmic reticulum stress in immunity. Annu Rev Immunol 33:107–138. https://doi.org/10.1146/annurev-immunol-032414-112116
8. Frakes AE, Dillin A (2017) The UPR(ER): sensor and coordinator of organismal homeostasis. Mol Cell 66(6):761–771. https://doi.org/10.1016/j.molcel.2017.05.031

9. Tufanli O, TelkoparanAkillilar P, Acosta-Alvear D et al (2017) Targeting IRE1 with small molecules counteracts progression of atherosclerosis. Proc Natl Acad Sci USA 114(8):E1395–E1404. https://doi.org/10.1073/pnas.1621188114
10. Azim MHS (1979) Glycoprotein synthesis and inhibition of glycosylation by tunicamycin in preimplantation mouse embryos: compaction and trophoblast adhesion. Cell 1979(18):217–227
11. Figueroa-Juarez E, Noriega LG, Perez-Monter C et al (2021) The role of the unfolded protein response on renal lipogenesis in C57BL/6 mice. Biomolecules. https://doi.org/10.3390/biom11010073
12. Cheng C, Ru P, Geng F et al (2015) Glucose-mediated N-glycosylation of SCAP is essential for SREBP-1 activation and tumor growth. Cancer Cell 28(5):569–581. https://doi.org/10.1016/j.ccell.2015.09.021
13. Han J, Kaufman RJ (2016) The role of ER stress in lipid metabolism and lipotoxicity. J Lipid Res 57(8):1329–1338. https://doi.org/10.1194/jlr.R067595
14. Gao M, Monian P, Pan Q, Zhang W, Xiang J, Jiang X (2016) Ferroptosis is an autophagic cell death process. Cell Res 26(9):1021–1032. https://doi.org/10.1038/cr.2016.95
15. Muir A, Danai LV, Gui DY, Waingarten CY, Lewis CA, Vander Heiden MG (2017) Environmental cystine drives glutamine anaplerosis and sensitizes cancer cells to glutaminase inhibition. Elife. https://doi.org/10.7554/eLife.27713
16. Yang WS, Stockwell BR (2016) Ferroptosis: death by lipid peroxidation. Trends Cell Biol 26(3):165–176. https://doi.org/10.1016/j.tcb.2015.10.014
17. Xie Y, Hou W, Song X et al (2016) Ferroptosis: process and function. Cell Death Differ 23(3):369–379. https://doi.org/10.1038/cdd.2015.158
18. Doll S, Freitas FP, Shah R et al (2019) FSP1 is a glutathione-independent ferroptosis suppressor. Nature 575(7784):693–698. https://doi.org/10.1038/s41586-019-1707-0
19. Stockwell BR, Friedmann Angeli JP, Bayir H et al (2017) Ferroptosis: a regulated cell death nexus linking metabolism, redox biology, and disease. Cell 171(2):273–285. https://doi.org/10.1016/j.cell.2017.09.021
20. Brown CW, Amante JJ, Chhoy P et al (2019) Prominin2 drives ferroptosis resistance by stimulating iron export. Dev Cell 51(5):575-586 e4. https://doi.org/10.1016/j.devcel.2019.10.007
21. Xu C, Sun S, Johnson T et al (2021) The glutathione peroxidase Gpx4 prevents lipid peroxidation and ferroptosis to sustain Treg cell activation and suppression of antitumor immunity. Cell Rep 35(11):109235. https://doi.org/10.1016/j.celrep.2021.109235
22. Tang D, Chen X, Kang R, Kroemer G (2021) Ferroptosis: molecular mechanisms and health implications. Cell Res 31(2):107–125. https://doi.org/10.1038/s41422-020-00441-1
23. Schinzel RT, Higuchi-Sanabria R, Shalem O et al (2019) The hyaluronidase, TMEM2, promotes ER homeostasis and longevity independent of the UPR(ER). Cell 179(6):1306-1318 e18. https://doi.org/10.1016/j.cell.2019.10.018
24. Li B, Li C, Guo M et al (2018) Predictive value of LDH kinetics in bevacizumab treatment and survival of patients with advanced NSCLC. Onco Targets Ther 11:6287–6294. https://doi.org/10.2147/OTT.S171566
25. Aregger M, Lawson KA, Billmann M et al (2020) Systematic mapping of genetic interactions for de novo fatty acid synthesis identifies C12orf49 as a regulator of lipid metabolism. Nat Metab 2(6):499–513. https://doi.org/10.1038/s42255-020-0211-z
26. Urata S, Yun N, Pasquato A, Paessler S, Kunz S, de la Torre JC (2011) Antiviral activity of a small-molecule inhibitor of arenavirus glycoprotein processing by the cellular site 1 protease. J Virol 85(2):795–803. https://doi.org/10.1128/JVI.02019-10
27. Geng F, Cheng X, Wu X et al (2016) Inhibition of SOAT1 suppresses glioblastoma growth via blocking SREBP-1-mediated lipogenesis. Clin Cancer Res 22(21):5337–5348. https://doi.org/10.1158/1078-0432.CCR-15-2973
28. Davidson RC, Nett JH, Renfer E et al (2004) Functional analysis of the ALG3 gene encoding the Dol-P-Man: Man5GlcNAc2-PP-Dol mannosyltransferase enzyme of P. pastoris. Glycobiology 14(5):399–407. https://doi.org/10.1093/glycob/cwh023
29. Maurel M, Samali A, Chevet E (2014) Endoplasmic reticulum stress: at the crossroads of inflammation and metabolism in hepatocellular carcinoma development. Cancer Cell 26(3):301–303. https://doi.org/10.1016/j.ccr.2014.08.007
30. Keestra-Gounder AM, Byndloss MX, Seyffert N et al (2016) NOD1 and NOD2 signalling links ER stress with inflammation. Nature 532(7599):394–397. https://doi.org/10.1038/nature17631
31. Spiteller G, Afzal M (2014) The action of peroxyl radicals, powerful deleterious reagents, explains why neither cholesterol nor saturated fatty acids cause atherogenesis and age-related diseases. Chemistry 20(46):14928–14945. https://doi.org/10.1002/chem.201404383
32. Hadian K, Stockwell BR (2020) SnapShot: ferroptosis. Cell 181(5):1188-1188 e1. https://doi.org/10.1016/j.cell.2020.04.039
33. Dixon SJ, Lemberg KM, Lamprecht MR et al (2012) Ferroptosis: an iron-dependent form of nonapoptotic cell death. Cell 149(5):1060–1072. https://doi.org/10.1016/j.cell.2012.03.042
34. Zeng C, Tang H, Chen H, Li M, Xiong D (2020) Ferroptosis: a new approach for immunotherapy. Cell Death Discov 6(1):122. https://doi.org/10.1038/s41420-020-00355-2
35. Wang W, Green M, Choi JE et al (2019) CD8(+) T cells regulate tumour ferroptosis during cancer immunotherapy. Nature 569(7755):270–274. https://doi.org/10.1038/s41586-019-1170-y
36. Liu X, Bao X, Hu M et al (2020) Inhibition of PCSK9 potentiates immune checkpoint therapy for cancer. Nature 588(7839):693–698. https://doi.org/10.1038/s41586-020-2911-7
37. Hogquist KA, Jameson SC, Heath WR, Howard JL, Bevan MJ, Carbone FR (1994) T cell receptor antagonist peptides induce positive selection. Cell 76(1):17–27. https://doi.org/10.1016/0092-8674(94)90169-4
38. Himmelreich N, Dimitrov B, Geiger V et al (2019) Novel variants and clinical symptoms in four new ALG3-CDG patients, review of the literature, and identification of AAGRP-ALG3 as a novel ALG3 variant with alanine and glycine-rich N-terminus. Hum Mutat 40(7):938–951. https://doi.org/10.1002/humu.23764
39. Ke SB, Qiu H, Chen JM et al (2020) ALG3 contributes to the malignancy of non-small cell lung cancer and is negatively regulated by MiR-98-5p. Pathol Res Pract 216(3):152761. https://doi.org/10.1016/j.prp.2019.152761
40. Zhou H, Cao T, Li WP, Wu G (2019) Combined expression and prognostic significance of PPFIA1 and ALG3 in head and neck squamous cell carcinoma. Mol Biol Rep 46(3):2693–2701. https://doi.org/10.1007/s11033-019-04712-y
41. Li Y, Weng Y, Pan Y et al (2021) A novel prognostic signature based on metabolism-related genes to predict survival and guide personalized treatment for head and neck squamous carcinoma. Front Oncol 11:685026. https://doi.org/10.3389/fonc.2021.685026
42. Sun X, He Z, Guo L et al (2021) ALG3 contributes to stemness and radioresistance through regulating glycosylation of TGF-beta receptor II in breast cancer. J Exp Clin Cancer Res 40(1):149. https://doi.org/10.1186/s13046-021-01932-8
43. Friedmann Angeli JP, Krysko DV, Conrad M (2019) Ferroptosis at the crossroads of cancer-acquired drug resistance and immune evasion. Nat Rev Cancer 19(7):405–414. https://doi.org/10.1038/s41568-019-0149-1
44. Lee HH, Wang YN, Xia W et al (2019) Removal of N-linked glycosylation enhances PD-L1 detection and predicts anti-PD-1/PD-L1 therapeutic efficacy. Cancer Cell 36(2):168-178 e4. https://doi.org/10.1016/j.ccell.2019.06.008

45. Cha JH, Yang WH, Xia W et al (2018) Metformin promotes antitumor immunity via endoplasmic-reticulum-associated degradation of PD-L1. Mol Cell 71(4):606-620 e7. https://doi.org/10.1016/j.molcel.2018.07.030
46. Li CW, Lim SO, Xia W et al (2016) Glycosylation and stabilization of programmed death ligand-1 suppresses T-cell activity. Nat Commun 7:12632. https://doi.org/10.1038/ncomms12632
47. Dunn WB, Broadhurst D, Begley P et al (2011) Procedures for large-scale metabolic profiling of serum and plasma using gas chromatography and liquid chromatography coupled to mass spectrometry. Nat Protoc 6(7):1060–1083. https://doi.org/10.1038/nprot.2011.335
48. Sarafian MH, Gaudin M, Lewis MR et al (2014) Objective set of criteria for optimization of sample preparation procedures for ultra-high throughput untargeted blood plasma lipid profiling by ultra performance liquid chromatography-mass spectrometry. Anal Chem 86(12):5766–5774. https://doi.org/10.1021/ac500317c